IEEE Photonics Journal
An IEEE Photonics Society Publication

Open Access

Waveguide Engineering of Graphene Optoelectronics—Modulators and Polarizers

Volume 10, Number 1, February 2018

Yuan Meng
Shengwei Ye
Yijie Shen
Qirong Xiao
Xing Fu
Rongguo Lu
Yong Liu, *Senior Member, IEEE*
Mali Gong

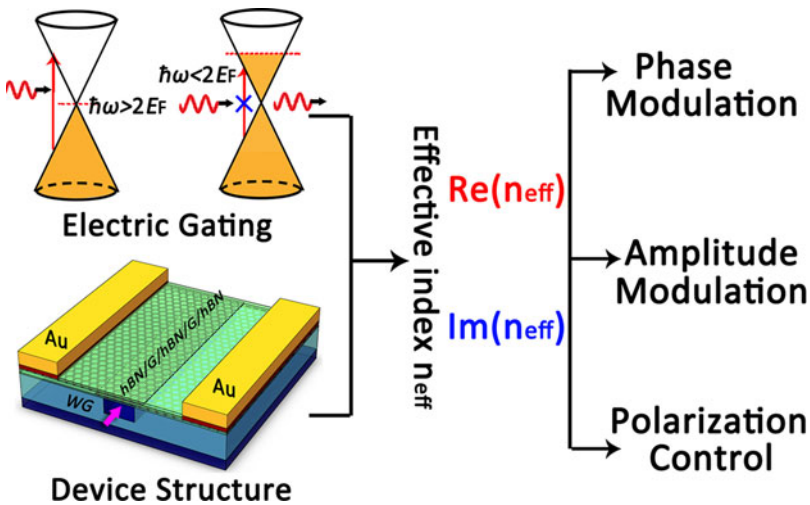

DOI: 10.1109/JPHOT.2018.2789894
1943-0655

Waveguide Engineering of Graphene Optoelectronics—Modulators and Polarizers

Yuan Meng,[1] Shengwei Ye,[2] Yijie Shen,[1] Qirong Xiao,[1] Xing Fu,[1] Rongguo Lu,[2] Yong Liu,[2] *Senior Member, IEEE*, and Mali Gong[1]

[1]State Key Laboratory of Precision Measurement Technology and Instruments, Department of Precision Instrument,Tsinghua University, Beijing 100084, China
[2]State Key Laboratory of Electronic Thin Films and Integrated Devices, School of Optoelectronic Information, University of Electronic Science and Technology of China, Chengdu 610054, China

DOI:10.1109/JPHOT.2018.2789894

Manuscript received October 3, 2017; revised December 29, 2017; accepted January 1, 2018. Date of publication January 9, 2018; date of current version January 25, 2018. This work was supported by the National Natural Science Foundation of China under Grants 61435010, 61421002, and 61307070, and Fundamental Research Funds for the Central Universities under Grant ZYGX2016J070. Corresponding author: Mali Gong (e-mail: gongml@mail.tsinghua.edu.cn).
This paper has supplementary downloadable material available at http://ieeexplore.ieee.org.

Abstract: The concept of incorporating graphene into nanophotonic waveguides has pullulated into massive broadband optoelectronic applications with compact footprint. We theoretically demonstrate that by solely altering the dimension design of graphene-laminated silicon waveguides, the phase, amplitude, and polarization of the fundamental propagating modes can all be effectively tailored under different bias voltages. Different device functionalities, including optical amplitude/phase modulators and polarizers, are ascribed into the devising of the effective mode index. A comprehensive analysis and unified design scenarios upon waveguide geometries are summarized, with fabrication robustness and moderate process complexity. Moreover, design examples are manifested. We report a TM-mode-based phase modulator, achieving a π phase shift within an active length of 49.2 μm with dual graphene layers. A feasible polarization-independent amplitude modulator is also demonstrated, where the discrepancy of the imaginary parts of the effective mode index between the two fundamental modes is kept at an order of 10^{-5} over a broad wavelength range from 1.35 to 1.65 μm.

Index Terms: Graphene, integrated optics devices, modulators, optoelectronics, waveguides.

1. Introduction

Recent years have witnessed the significant role that silicon photonics can play in realizing ultrafast network interconnects with low power dissipation [1], [2], on-chip signal processing [3] and massive other emerging applications. Optical modulators are the crucial components for tailoring the fundamental properties of light, such as amplitude, phase or polarization [1]. Conventional silicon modulators exploiting plasma dispersion effect [4] generally suffer from large footprints.

Resonant configurations like microrings may largely miniaturize device footprint [5], but at the cost of intrinsically narrowed bandwidth. They are also sensitive to temperature fluctuations and difficult to implement. Moreover, thermal-optic modulators [6] commonly encounter challenges in thermal crosstalk and relatively slow operation speed, while electro-optic modulators [7], [8] are generally occupied in adopting sophisticated structures or complicated fabrication processes to meet the ever-increasing bandwidth requirements.

At present, the advancement toward further integrated photonic circuits encounters stumbling blocks in dimensional scaling and accommodation with present electronics [9]. Consequently, novel structures and materials are required to be explored to handle these problems. Integrated optical modulators for chip-scale interconnects [10] are supposed to possess compact footprint, broad bandwidth, high operation speed, low energy consumption and compatibility with CMOS platform.

Meanwhile, graphene along with a family of two-dimensional materials [11] has stood out as a prominent star in the horizon of photonics and electronics, attracting tremendous research interest for its exceptional optical and electrical attributes [12]. As a monolayer of carbon atoms arranged in a hexagonal lattice, graphene enjoys ultrahigh electron mobility [13], strong interactions with light [14], excellent thermal conductivity [15], giant optical nonlinearity [16] and high flexibility. Moreover, the gapless, linear band structure makes it a broadband absorber from visible to infrared range [17]. By shifting the Fermi level, one can effectively control graphene's optical absorptions [18]. These unique properties make graphene a promising candidate of active material for realizing novel optical modulators [19]–[22] and have also been proven fruitful for plenty of broadband and ultracompact applications like polarizers [23]–[25], photodetectors [26], and sensors [27].

Here a comprehensive analysis upon graphene-integrated nanophotonic waveguides is presented. We theoretically demonstrate that the phase, amplitude and polarization of the fundamental propagating modes can be effectively tailored within graphene-hybrid silicon waveguides, by just altering the waveguide dimension design and bias voltages. We ascribe different device functionalities, including optical amplitude/phase modulators and polarizers, into the variation of a single fundamental parameter: the effective mode index. The device structure design recipes, fabrication processes, and operation principles are synthetically discussed. Moreover, the proposed graphene modulator can flexibly switch between amplitude and phase modulation under different bias voltages. A TM mode phase modulator under anisotropic graphene model is reported with moderate process complexity, where a π phase shift is achieved in an active length of 49.2 μm. Furthermore, a polarization-independent amplitude optical modulator is demonstrated, with extremely approaching modulation strength between the two fundamental modes over a broad wavelength range from 1.35 to 1.65 μm.

2. Fundamentals

2.1 Optoelectronic Properties of Graphene

As the electrons of graphene possess low density of states within a single atomic layer [17], [18], the Fermi level E_F or chemical potential μ of graphene can be remarkably tuned when the carrier density is altered. Consequently, when we apply a bias voltage V to graphene capacitors, the carriers will be accumulated and μ is then effectively controlled by electrical gating [28]–[31],

$$\mu = \hbar v_F \sqrt{\pi \frac{\varepsilon_0 \varepsilon_r}{d_{s1} e} |V - V_0|} \tag{1}$$

where $\hbar$ is the reduced Planck constant and v_F stands for Fermi velocity [12]; ε_r is the relative permittivity of the insulation layer; d_{s1} represents the thickness of the insulating spacer [19]; e is the elementary electric charge and V_0 is the offset voltage relating to the natural doping of graphene samples.

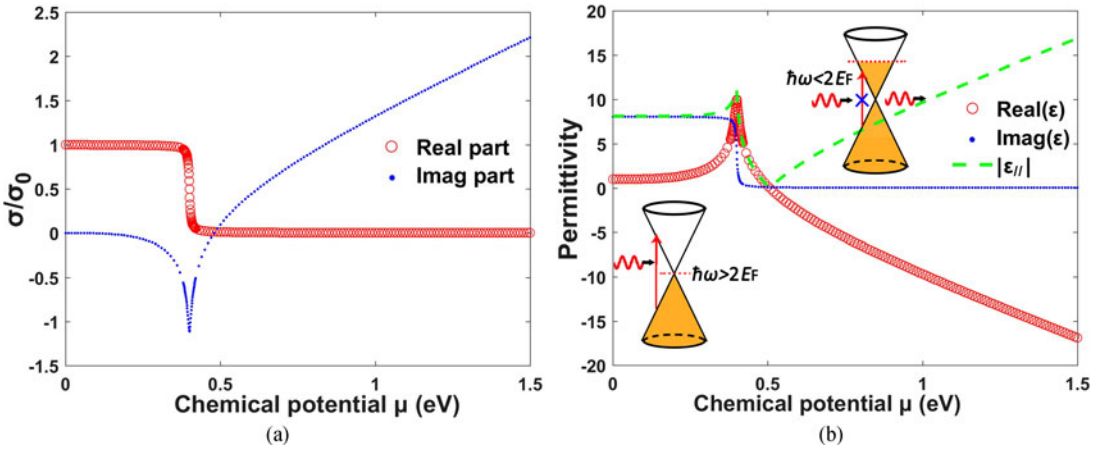

Fig. 1. Complex surface conductivity (a) and permittivity (b) of graphene as a function of chemical potential μ, under light wavelength $\lambda = 1550$ nm at room temperature $T = 296$ K.

The surface conductivity of graphene $\sigma_{||}$ can be deduced from Kubo formula [32], [33] as a complex form comprised of intra- and inter- band contributions [1], [34]–[36]

$$\sigma_{||}(\mu) = \sigma_0 \frac{4\mu}{\pi\hbar(\Gamma - i\omega)} + \sigma_0 \left\{ 1 + \frac{1}{\pi} \arctan \frac{\hbar\omega - 2\mu}{\hbar\Gamma} - \frac{1}{\pi} \arctan \frac{\hbar\omega + 2\mu}{\hbar\Gamma} - \frac{i}{2\pi} \ln \left[\frac{(\hbar\omega + 2\mu)^2 + (\hbar\Gamma)^2}{(\hbar\omega - 2\mu)^2 + (\hbar\Gamma)^2} \right] \right\} \tag{2}$$

where the first addition item represents intraband conductivity; the second corresponds for interband conductivity. ω is angular frequency and $\hbar\Gamma = 5$ meV [37]–[40] is the charged particle scattering rate. Fig. 1(a) illustrates the complex surface conductivity of graphene as a function of μ in room temperature at a signal wavelength of $\lambda = 1.55$ μm. $\sigma_0 = e^2/(4\hbar) = 60.85$ μS is the optical conductivity of undoped graphene. The equivalent in-plane permittivity $\varepsilon_{||}$ can be formulated as [40]

$$\varepsilon_{||} = 1 + i\sigma_{||}/(\omega\varepsilon_0 d_g) \tag{3}$$

where ε_0 is the vacuum permittivity and $d_g = 0.7$ nm is the equivalent thickness of graphene monolayer [19]–[22], [37].

A dramatic variation in graphene's surface conductivity can be observed when μ is tuned above 0.4 eV, as a consequence of Pauli blocking [17], [18]. As is illustrated in Fig. 1(b) inset, for communication wavelengths, interband absorption is dominating for graphene. When μ is tuned around the Dirac point, both interband and intraband transitions can take place and graphene exhibits broadband absorption. However, when μ is shifted to a higher value that $|\mu| > \hbar\omega/2$, all empty states at conduction band are occupied and interband transitions get blocked, resulting in a significant drop of optical absorption for graphene. Moreover, the absolute value of graphene's in-plane permittivity $|\varepsilon_{||}|$ approaches zero when $\mu \approx 0.5$ eV, and then graphene transfers from dielectric to metallic response.

2.2 Graphene-Integrated Photonic Waveguides

Since large-area and high-quality graphene can be effectively synthesized on metal foils [41], wafer-scale processes of transferring and patterning graphene onto arbitrary substrates are achievable [42]. Hence, one of the most efficacious way of putting graphene into optoelectronic devices is to incorporate it with nanophotonic waveguides, which is the elementary building block for integrated photonic circuits. However, the following problems still exist.

(1) Isotropic model of graphene. Since the first experimental demonstration of a broadband graphene modulator [19], plenty of amelioration approaches have been theoretically proposed.

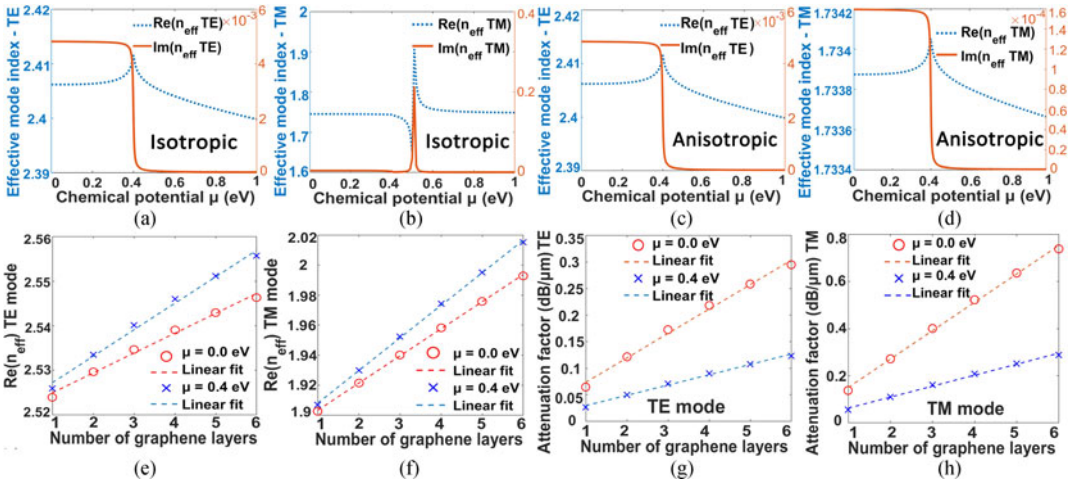

Fig. 2. Comparison of isotropic/anisotropic graphene model and the impact of graphene layers upon n_{eff}. (a) and (b) Re(n_{eff}) and Im(n_{eff}) under the isotropic graphene model for quasi-TE and TM modes, respectively. A dramatically enhanced absorption takes place around $\mu \approx 0.5$ eV for the TM mode [24], [34]–[36], [52]. (c) and (d) The same for the anisotropic graphene model. (e) and (f) Re(n_{eff}) as a function of the number of graphene layers under the anisotropic graphene model for TE and TM modes, respectively. (g) and (h) Normalized attenuation factors for TE and TM modes, respectively. The waveguide dimension is 500 nm $\times$ 250 nm. Simulation details are elaborated in the Supplementary Material.

However, in some simulations [24], [34]–[36] graphene was actually treated as isotropic thin sheets, leading to a phenomenon that the electric field of TM mode strongly concentrates in graphene when the chemical potential μ is tuned about 0.5 eV [24]. As is illustrated in Fig. 2(b), graphene exhibits extremely enhanced absorption for fundamental TM mode. This epsilon-near-zero effect [34] actually originates from the isotropic model of graphene, as the absolute value of graphene's in-plane permittivity $|\varepsilon_{||}|$ approaches zero when $\mu \approx 0.5$ eV. However, considering the two-dimensional nature that graphene's electrons are tightly confined within the atomic monolayer [20], graphene is virtually anisotropic [25], [43]–[46]. While the in plane permittivity $\varepsilon_{||}$ can be tuned near zero by bias voltages, the surface-normal component $\varepsilon_{\perp}$ stays constant [30], [44], [45]. Then the dramatically enhanced light absorption will not occur any more, as shown in Fig. 2(d). Consequently, anisotropic graphene model should be applied instead.

(2) Device fabrications. Although graphene exhibits remarkably high light absorption, its miniscule thickness still poses limitations. Several proposals are put forward to further enhance its interaction with electromagnetic fields, by embedding multiple graphene layers into waveguide core [24], [34]–[36], [45], or applying resonant cavities like microrings [21], [47]. However, some concepts of the first approach are quite challenging and somewhat not cost-effective to implement. As crystalline silicon may not be regrown on top of graphene stacks with the manufacturing technology available at present, the embedded designs might just possibly find the way to have polysilicon deposited [9] and patterned afterwards, which largely complicates the fabrication process and will introduce additional loss [20]. Moreover, despite that both Re(n_{eff}) and Im(n_{eff}) increase quasi-linearly with the number of graphene flakes, as shown in Fig. 2(e)–(h), the electrical contacts and the bias voltages are difficult to implement effectively if more than two graphene layers (sandwiched by isolation layers) are vertically stacked [9]. Consequently, incorporating multiple graphene flakes into the center of a waveguide [45] is more challenging, and not cost-effective in terms of multiplied process complexity.

For ring resonator configurations [21], beside the aforementioned sophisticated design and fabrication requirements, the broadband characteristic is sacrificed, which is one of the most intriguing properties of graphene. Therefore, theoretical designs should bear practicability with actual fabrication process. The device manufacture must be reproducible, having acceptable complexity and compatibility with current semiconductor platform [9], [48].

(3) Scattered explorations. Based on the coupling between graphene and photonic waveguides or optical fibers, plenty of applications like modulators [19]–[21] and polarizers [23]–[25] are reported. However, a comprehensive investigation accommodating different devices functionalities still remains elusive. Hence, in this paper an in-depth analysis with unified device design criteria including amplitude/phase modulation and polarization control is presented.

(4) Polarization-dependent modulators. Owing to the anisotropic feature of graphene and the polarization-dependent modal distributions, the absorption of graphene is sensitive to polarization states. This property can be utilized to realize broadband polarizers [23] or optical sensors [49]. However, it also makes the graphene-on-waveguide modulators virtually polarization-dependent, accompanied by extra inconvenience in optical alignments [30] or accessorial insertion loss from polarizers. Nevertheless, recently proposed polarization-independent modulators, where partly tilted [50] or entirely circumfused graphene configurations [51] are applied, are either highly sensitive to fabrication errors or not feasible for actual device manufactures.

Consequently, these issues will be addressed in this paper. A TM-mode-based phase modulator, which is free from previously proposed complex embedded structures [52]–[54] under anisotropic graphene model, and a polarization- independent modulator with fabrication feasibility are also presented latter.

2.3 Waveguide Engineering for Graphene

When integrated with optical waveguides, graphene strongly interacts with the propagating modes and influences the complex effective mode index n_{eff}. The real part $\text{Re}(n_{\text{eff}})$ corresponds to electro-refraction [54] and the imaginary part $\text{Im}(n_{\text{eff}})$ manifests electro-absorption. The anisotropic dielectric constant of graphene [43]–[46] can be formulated as a diagonal tensor [25] (see Section 1 of the Supplementary Material). The in-plane permittivity $\varepsilon_{||}$ can be effectively tuned by electrostatics, while the perpendicular component $\varepsilon_{\perp} = 2.5$ (retrieved from graphite [30], [44]) remains unchanged against chemical potential μ.

Since graphene only interacts with the tangential electric filed $\boldsymbol{E}_{||}$ that is parallel to its flake plane [19], [38], the surface current density can be formulated according to the differential form of Ohm's law,

$$\boldsymbol{J}_{\boldsymbol{s}} = \hat{\boldsymbol{n}} \times (\boldsymbol{H}_1 - \boldsymbol{H}_2) = \sigma_{||} \boldsymbol{E}_{||} \tag{4}$$

where $\hat{\boldsymbol{n}}$ represents the unit normal vector at the boundary of graphene film, and (4) remains as another paradigm to formulate anisotropic graphene via utilizing its surface conductivity [55]. Accordingly, the time-averaged power dissipation density $\langle p \rangle$ can be obtained [38].

$$\langle p \rangle = \langle \boldsymbol{J}_{\boldsymbol{s}} \cdot \boldsymbol{E}_{||} \rangle = \langle \sigma_{||} \boldsymbol{E}_{||} \cdot \boldsymbol{E}_{||} \rangle = \sigma_{||} |\boldsymbol{E}_{||}|^2 / 2 \tag{5}$$

Consequently, if one desires for enhanced graphene absorption with respect to amplitude modulators and polarizers, the mode overlap between the evanescent in-plane electric field and graphene shall be maximized.

Although several plasmonic approaches [34], [56] are proposed to enhance modulation strengths, they generally inherit the high Ohmic loss from metal. Our proposal is to solely tailor the width and height of graphene-laminated photonic waveguides, which can be easily implemented by standard lithography for SOI wafers with different thickness of top Si layer. Then the functionalities of phase/amplitude modulation and polarization control can all be selectively achieved via standard semiconductor platform.

3. Device Design and Manufacture

3.1 Device Structure

For the sake of acceptable process complexity and effective electrical gating, configurations with single or double graphene layers are promising for future market feasibility. However, for monolayer graphene configuration [19], the extinction ratio per micron remains compromised. Moreover, the

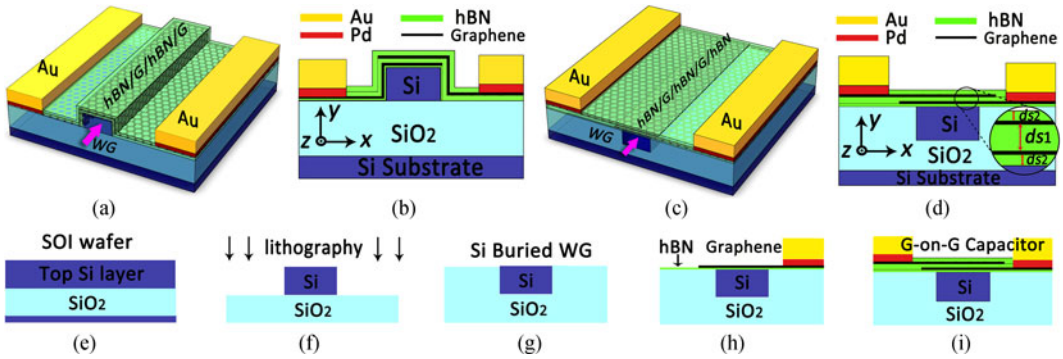

Fig. 3. Device structure sketch. (a) and (b) Convex strip waveguide in graphene–insulator–graphene configuration. (c) and (d) Buried waveguide in planner surface architecture. (e)–(i) Corresponding device fabrication process of the buried structure (bottom Si substrate is not revealed) by two steps of transfer. Undesired regions can be removed via oxygen plasma and patterned by electron beam lithography [20], [58].

Si waveguide needs to be doped to serve as a back gate, which will deteriorate carrier mobility and introduce an extra loss from free career absorption. By contrast, graphene-insulator-graphene capacitor structure is more promising [20], for its doubled graphene-light interaction strength, reduced loss and increased operation speed.

A set of full-vector simulations via Finite Element Method (FEM) are conducted. Fig. 3 illustrates two classical structures of photonic waveguides integrated with dual graphene layers. Compared with the first configuration of convex strip waveguide [20], the buried waveguide structure allows for co-planner processing, for the CVD grown graphene flakes can be effectively transferred to arbitrary topological surfaces [42] at wafer scale with flat interfaces [57], [58]. However, exact transfer of graphene upon complex architectures like Fig. 3(b) are generally compromised in actual fabrication processes.

Consequently, the buried waveguide structure in Fig. 3(c) is adopted. Hexagonal boron nitride (hBN) is selected as the isolation material rather than Al_2O_3, for it can maintain graphene's high mobility compared with oxides and can reduce the total capacitance-resistance (RC) time constant [59], [60]. As is shown in Fig. 3(e)–(i), the proposed devices are based upon commercial SOI wafers, which is then planarized with oxide after lithography. The dual graphene layers can be implemented via a two-step transfer [9] to mitigate transfer-related defects. The first is CVD-grown graphene/hBN stack, and the second is hBN/graphene/hBN layers. The Pd/Au electrodes are evaporated to form electrical contacts to graphene for the low contact resistance it can provide [61].

3.2 Fabrication Parameters

The scatter rate $\hbar\Gamma$ of graphene is influenced by sample quality [37], as imperfections in growth and transfer process will lead to a larger value of $\hbar\Gamma$. As is illustrated in Fig. 4, for an exemplary 500 nm $\times$ 260 nm waveguide dimension under the configuration shown as Fig. 3(d) (see Section 2 of the Supplementary Material for details), a larger scatter rate results in larger absorption when interband transitions are blocked at a higher chemical potential of $\mu > 0.4$ eV for $\lambda = 1550$ nm. Meanwhile, comparatively milder variations in the effective mode index n_{eff} are observed around $\mu = 0.4$ eV for both TE and TM modes at larger scatter rates. A typical value of $\hbar\Gamma = 5$ meV [37]–[39] is applied in the following simulations.

Meanwhile, the thickness of spacer layer also exerts significant influence on device performance. As is shown in Fig. 3(d), the interval between two graphene layers is defined as d_{s1}, while the thicknesses of the bottom and top isolation layers are set identically as d_{s2}. Fig. 5 illustrates the different impact of the two parameters on n_{eff} under the same exemplary device structure shown as Fig. 4. According to (1), d_{s1} influences the mapping between μ and applied voltage V. Meanwhile, the capacitance C_g of the dual graphene structure is also effected as $C_g = \varepsilon_0\varepsilon_r S/d_{s1}$, where ε_r is the

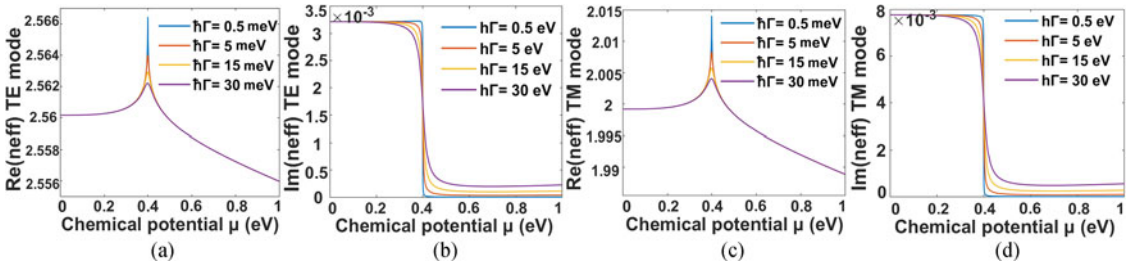

Fig. 4. Impact of graphene's scatter rate on n_{eff}. (a) and (b) Re(n_{eff}) and Im(n_{eff}) for the TE mode. (c) and (d) The same for the TM mode. The simulations are conducted via the FEM solver of COMSOL. Simulation details are in the Supplementary Material.

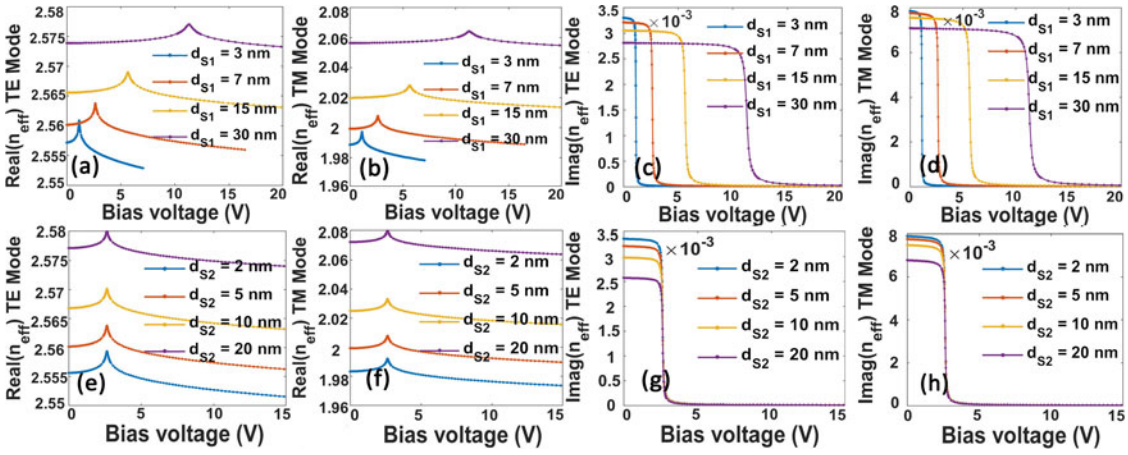

Fig. 5. Impact of spacer layer thickness. (a) and (b) Re(n_{eff}) as a function of bias voltage under different capacitor plates interval d_{s1} for TE and TM modes, respectively. (c) and (d) The same for Im(n_{eff}). (e) and (f) Re(n_{eff}) under different values of d_{s2} for TE and TM modes, respectively. (g) and (h) The same for Im(n_{eff}).

permittivity of spacer layer, and S is the overlapped area of the two graphene films that serves as capacitor plates. Hence, as is shown in Fig. 5(a)–(d), a smaller d_{s1} leads to a reduced amount of bias voltage for achieving a given value of μ, which is favorable for the low power consumption required in chip-scale optical interconnects. However, an enlarged capacitance brings about a larger RC delay, degrading the operation speed and electrical bandwidth. Consequently, a trade-off appears and the determination of d_{s1} should be based upon specific design target. If one argues for a higher modulation speed, a thicker isolation layer can be selected. Otherwise, a smaller d_{s1} is expected, assuming that the energy consumption is more emphasized.

By contrast, the value of d_{s2} has little impact upon power consumption and barely influence the total device capacitance. The bottom and top spacer layers are applied to encapsulate graphene from environmental contamination and provide electrical insulation. It mainly affects the intensity of the evanescent electric filed within graphene layers. Thus, generally d_{s2} is desired to be as small as possible to strengthen the optical absorption of graphene. In the following simulations, we set $d_{s1} = 7$ nm [19]–[22], [36], for a low power dissipation is pursued and a smaller value of $d_{s2} = 5$ nm with fabrication feasibility [37], [54].

3.3 Waveguide Dimension

The waveguide width can be determined via standard lithography process and the height can be altered by etching depth for SOI wafers with different thickness of top Si layers. By tailoring the

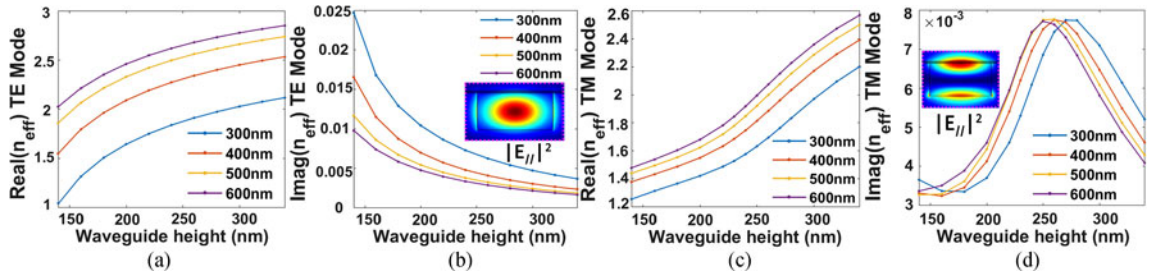

Fig. 6. Geometry variation for the buried waveguide structure with dual graphene layers at 1550 nm. (a) and (b) Re(n_{eff}) and Im(n_{eff}) for the fundamental TE mode, respectively. (c) and (d) The same for the fundamental TM mode. Inset: Intensity distributions of the tangential electric field $|\boldsymbol{E}_{||}|^2$ at a 500 nm $\times$ 260 nm buried waveguide for (b) TE and (d) TM modes.

dimensions of the graphene-integrated photonic waveguides, the effective mode index n_{eff} can be designed with flexibility.

Fig. 6 illustrates the variation of n_{eff} under different waveguide dimensions at $\mu = 0$ eV for the buried waveguide architecture shown in Fig. 3(c). According to Fig. 6(a) and (c), a larger waveguide cross-section intrinsically leads to a bigger Re(n_{eff}) for both TE and TM modes. However, the imaginary part Im(n_{eff}) exhibits distinctive variation trends as a direct result of the polarization-dependent mode distribution and the anisotropic nature of graphene. As is shown in Fig. 6(b) inset, the maximum intensity of the in-plane electric filed $|\boldsymbol{E}_{||}|^2$ locates at the center of the strip waveguide for TE mode. A weaker mode confinement from a smaller waveguide dimension leads to a stronger evanescent tail and increased mode overlap between $|\boldsymbol{E}_{||}|$ and graphene. Therefore, the optical absorption of graphene gets strengthened subsequently. However, the mode confinement factor for TE mode cannot be sacrificed without bridles to pursue light-graphene interaction enhancement. Although for fundamental TE mode, waveguides with smaller dimensions in Fig. 6(b) exhibit stronger absorption than TM mode, apart from soaring scatter loss, some of them are already below cut-off, as the real part of the effective mode index must satisfy $n_{\text{eff}} > n_{\text{cladding}}$ for guided modes.

By contrast, TM mode operation scheme is promising. Since the maximum intensity of $|\boldsymbol{E}_{||}|$ mainly distributes at the top and bottom surface of the buried strip waveguide, complex embedded structures are no longer needed and a good mode overlap is observed. Moreover, other waveguide architectures are also explored. Fig. S4 demonstrates the influence of waveguide dimension on n_{eff} for the convex strip waveguide configuration of Fig. 3(a). Two more possible waveguide architectures with dual graphene layers are also investigated, though they are somewhat difficult to implement. The simulation results are illustrated as Figs. S5 and S6 in the Supplementary Material. The conclusion remains the same: generally small dimensions for TE mode and optimized waveguide cross-sections for TM mode.

4. Fundamental Applications

By devising waveguide dimensions, both the real and imaginary part of the effective mode index n_{eff} can be effectively tailored to envisage different device functionalities. By maximizing Im(n_{eff}), electro-absorptive amplitude modulators can be optimized. If one can simultaneously suppress Im(n_{eff}) for the orthogonal polarization states, the functionality of a polarizer can be achieved. Moreover, for the applications of phase modulation, $\triangle$Re(n_{eff}) is supposed to be maximized. Consequently, the devise designs are then mainly ascribed to the optimization of n_{eff} for different applications.

4.1 Phase Modulation

Although graphene-based modulators are massively explored for its electro-absorptive attributes, the excellent potential to realize pure phase modulators at telecommunication band is not fully emphasized. Actually, the variation of effective mode index $\triangle$Re(n_{eff}) with chemical potential μ

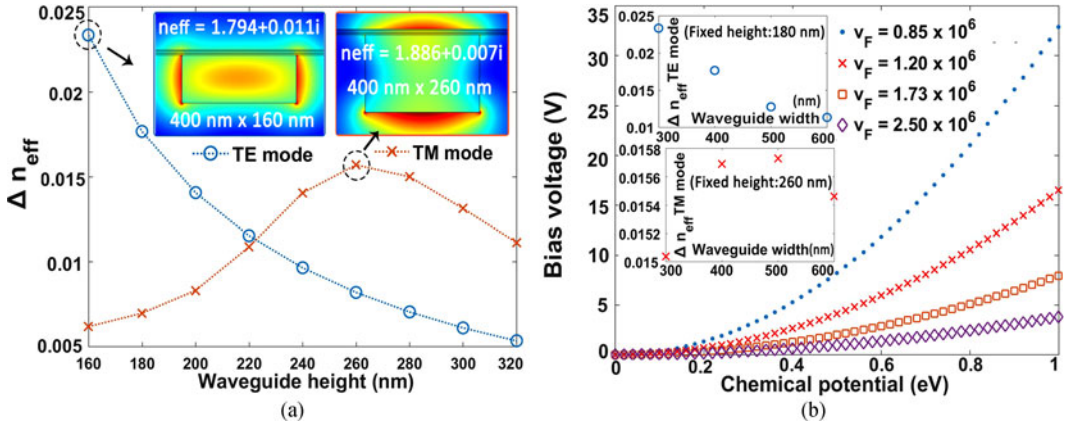

Fig. 7. (a) Dimension design of the buried waveguides structure shown as Fig. 3(c). The waveguide width is fixed as 400 nm. Inset: Distribution of electric field norm for two waveguide examples (marked in circle). (b) Applied voltage V as a function of μ under different Fermi velocities v_F of graphene. Inset: Variation of the effective mode indices at different waveguide widths for TE and TM modes, respectively.

in graphene-coupled photonic waveguides can approach 0.02, while conventional electro-optic materials may only induce a $\Delta\text{Re}(n_{\text{eff}})$ at the order of 10^{-4} [54], [62]. When μ is tuned to block interband transitions, the absorption of graphene is restrained at a low level and $\text{Re}(n_{\text{eff}})$ varies quasi-linearly with μ. Consequently, the phase of the propagating modes can be effectively modulated here, leaving the light amplitude almost unchanged at the same time.

For the sake of a compact footprint and ameliorated modulation strength, the variation $\Delta\text{Re}(n_{\text{eff}})$ should be maximized, and a small value of $\text{Im}(n_{\text{eff}})$, which corresponds to light attenuation, is desired. Fig. 7(a) and the inset panels in Fig. 7(b) illustrate the variations of $\Delta\text{Re}(n_{\text{eff}})$ at different waveguide dimensions for the buried waveguide architecture with dual graphene layers. Accordingly, a waveguide dimension of 500 nm $\times$ 260 nm is assigned for the fundamental TM mode. Although the 400 nm $\times$ 160 nm waveguide or other smaller waveguide architectures seem to exhibit larger $\Delta\text{Re}(n_{\text{eff}})$, they are actually very close to cut-off, where the losses are expected to surge. Consequently, we select a 400 nm $\times$ 180 nm dimension for TE mode. In addition, as one of the most fundamental parameters of graphene, the Fermi velocity v_F can be engineered as well, by modifying the graphene-embedded environment to improve electron-electron interactions [63]. Fig. 7(b) shows the relationship between bias voltage and chemical potential μ under different values of v_F [64], indicating that an enlarged v_F can be used to further decrease power consumption. Notably, one may hope to achieve a large $\Delta\text{Re}(n_{\text{eff}})$ while maintain a low value of its imaginary part at the same time to alleviate loss. Unfortunately, by combining Figs. 6 and 7, it can be noticed that a large value of $\Delta\text{Re}(n_{\text{eff}})$ is generally accompanied by a relatively large $\text{Im}(n_{\text{eff}})$. It denotes that the phase modulation efficiency and insertion loss may counteracts each other.

In Fig. 8(a) and (b) we plotted the effective mode index n_{eff} as a function of μ for TE and TM mode respectively. If we tune μ from 0.42 to 1.0 eV, the corresponding variations are observed as $\Delta\text{Re}(n_{\text{eff}}) = 0.0177$ (TE) and $\Delta\text{Re}(n_{\text{eff}}) = 0.0157$ (TM). As is illustrated in Fig. 8(c) and (d), a longer active length results in larger phase shift at a fixed $\Delta\mu$. Meanwhile, one can further mitigate the insertion loss of the proposed phase modulator by operating at a higher value of μ, as shown in Fig. 8(e) and (f). A π shift is achieved in a modulation length of $L_\pi = 43.8$ μm and 49.2 μm for TE and TM mode respectively. If we set an active length as 87.76 μm, the phase of the fundamental TE mode can be effectively altered from 0 to -2π by tuning μ from 0.42 to 1.0 eV, as shown in Fig. 8(g). Similarly, phase modulation can also be achieved in an active length of 98.54 μm for TM mode.

According to Fig. 8(g) and (h), it can be noticed that the minimum transmission rates of the phase modulator are not quite high: 0.75 and 0.89 for fundamental TE and TM mode respectively. This perturbation can be evaded by altering the operation points of μ. For instance, if we tune μ from

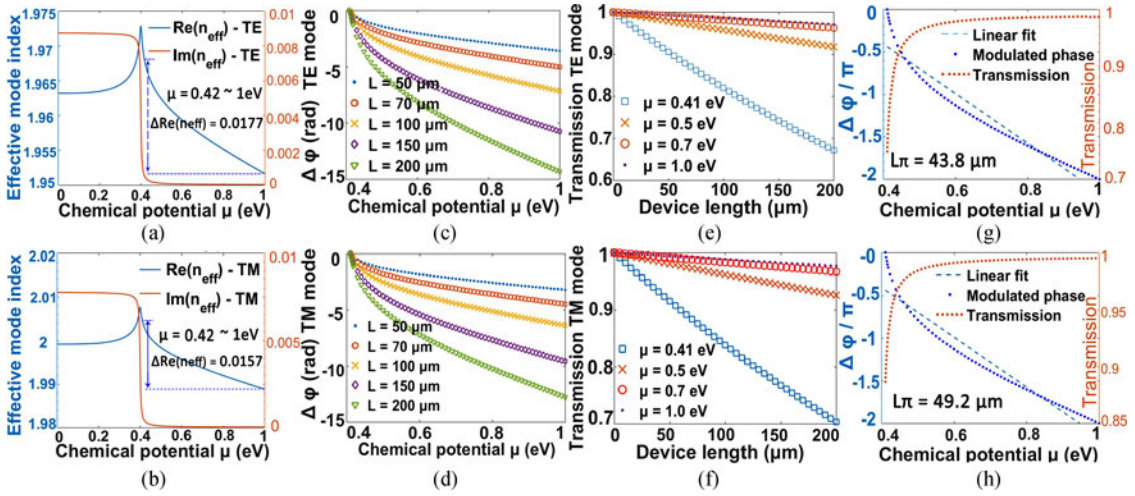

Fig. 8. Phase modulation for buried waveguide structures with dual graphene layers. (a) n_{eff} as function of μ for the fundamental TE mode under a waveguide dimension of 400 nm $\times$ 180 nm. (b) The same for the TM mode under a waveguide dimension of 500 nm $\times$ 260 nm. (c) and (d) Phase shift as a function of μ at different modulation lengths for TE and TM modes, respectively. (e) and (f) Transmission rate and insertion loss estimations versus μ for TE and TM modes, respectively. (g) Phase modulation performance and device transmission rate for an active length of 87.76 μm for the TE mode. (h) The same for the TM mode for an active length of 98.54 μm.

0.5 to 1.0 eV, the refractive index change is $\Delta\text{Re}(n_{\text{eff}})' = 0.011$ for TE mode, with a π phase shift attained at $L_\pi' = 69.8$ μm and corresponding transmission rate as 0.92–0.99, which barely varies the signal amplitude. Meanwhile, the minimum transmission for TM mode approximates 0.95 in this operation regime, with $\Delta\text{Re}(n_{\text{eff}})' = 0.010$ and $L_\pi' = 78.1$ μm (see Fig. S7 in Supplementary Material). Consequently, we believe TM mode operation is promising for phase modulation, for the mode confinement does not need to be largely sacrificed and is free from the additional losses when a waveguide is near cut-off. Moreover, unlike its TE-mode-based counterparts utilizing embedded structures, where polysilicon are required to be deposited, TM-mode-based phase modulators can be feasibly fabricated without extra process complexity.

4.2 Polarization Control

Integrated polarizers are of notable importance in in coherent optical communications. As an ultrathin anisotropic absorption medium, graphene can be integrated with Si waveguides or optical fibers to realize broadband polarizers [24], [65], [66]. Here we still propose for waveguide dimension engineering, exploiting the imaginary part of the effective mode index $\text{Im}(n_{\text{eff}})$ instead, to diminish a certain polarization state while holding the orthogonal one well guided with comparatively low loss.

The key of graphene-based polarizers is to magnify the discrepancy of $\text{Im}(n_{\text{eff}})$ between TE and TM mode. Fig. 9(a) and (d) illustrate the contrast of $\text{Im}(n_{\text{eff}})$ under different waveguide dimensions for the buried waveguide architecture sketched as Fig. 3(c). According to Fig. 9(a), waveguide dimensions that locate above the horizontal dashed line indicate that the $\text{Im}(n_{\text{eff}})$ of TE mode is larger than that of TM mode, manifesting a TM-pass behavior. However, those points that can no longer sustain guided TM mode must be excluded. Consequently, a waveguide dimension of 600 nm $\times$ 260 nm is selected for the TE-pass polarizer and 400 nm $\times$ 180 nm for TM-pass polarizer.

In Fig. 9(b) we plotted the calculated attenuation factors as a function of μ for the two fundamental modes. An extinction ratio of 10.8 dB is achieved for a 60 μm-long TE-pass polarizer and can be enlarged to 18.0 dB if a longer 100 μm graphene sheet is applied, as shown in Fig. 9(c). According to Fig. 9(e) and (f), a TM-pass polarizer can be attained in a 400 nm $\times$ 180 nm dimensioned waveguide similarly, and the extinction ratios are even higher: 11.2 dB at a device length of 60 μm and 18.6 dB for 100 μm length.

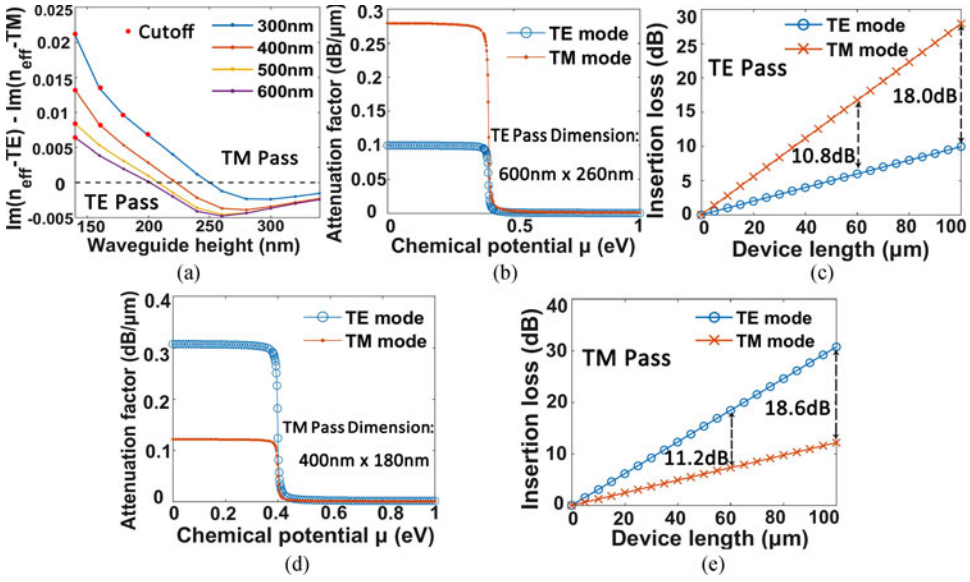

Fig. 9. Compact polarizers. (a) The difference between the imaginary parts of the effective mode index $\mathrm{Im}(n_{\mathrm{eff}})_{\mathrm{TE}} - \mathrm{Im}(n_{\mathrm{eff}})_{\mathrm{TM}}$ under different waveguide dimensions. (b) Attenuation factors versus μ for the TE mode. (c) Insertion loss versus graphene lengths for the TE mode. (d) and (e) The same for the TM mode.

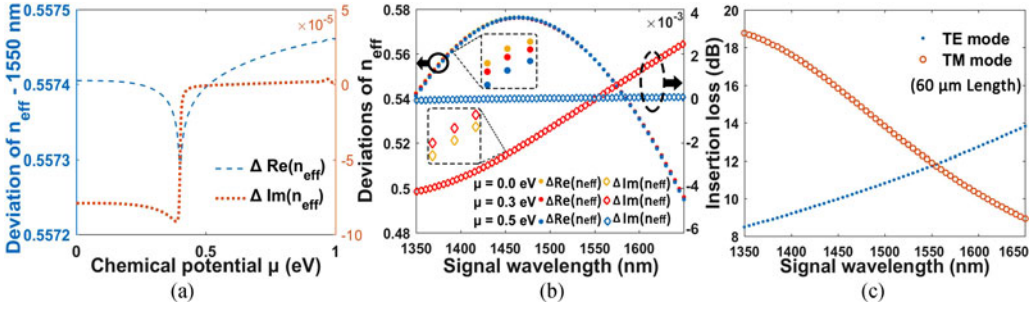

Fig. 10. Polarization-independent modulators for the buried waveguide structure. (a) Discrepancies of n_{eff} between fundamental TE and TM modes under $\mu = 0$ eV. (b) Discrepancies of $\mathrm{Re}(n_{\mathrm{eff}})$ and $\mathrm{Im}(n_{\mathrm{eff}})$ versus signal wavelengths λ at different μ. (c) Insertion loss for a 60-μm modulation length for TE and TM modes at $\mu = 0$ eV.

4.3 Amplitude Modulators

Graphene amplitude modulators without Mach-Zehnder configurations also exploit the strong optical absorption of graphene, which is essentially similar to the polarizers. The main difference is the electrically tuned interband absorptions for modulation. As is elaborated in the section of Fundamentals, we here investigate polarization-independent modulators. Two classical structures sketched in Fig. 3 are considered.

For the formerly discussed buried waveguide structure illustrated in Fig. 3(c), polarization-independent modulators may be realized by choosing a waveguide dimension with equal value of $\mathrm{Im}(n_{\mathrm{eff}})$ for TE and TM modes. According to Fig. 9(a) and (d), an exemplary 400 nm $\times$ 225 nm waveguide dimension is selected (see Supplementary Material). According to Fig. 10(a), the discrepancy of $\mathrm{Im}(n_{\mathrm{eff}})$ between the fundamental TE and TM mode is only at the order of 10^{-5} for $\lambda = 1550$ nm under $\mu = 0$ eV, denoting extremely approaching amplitude attenuations among two orthogonal polarization states. However, under this geometry the two fundamental modes

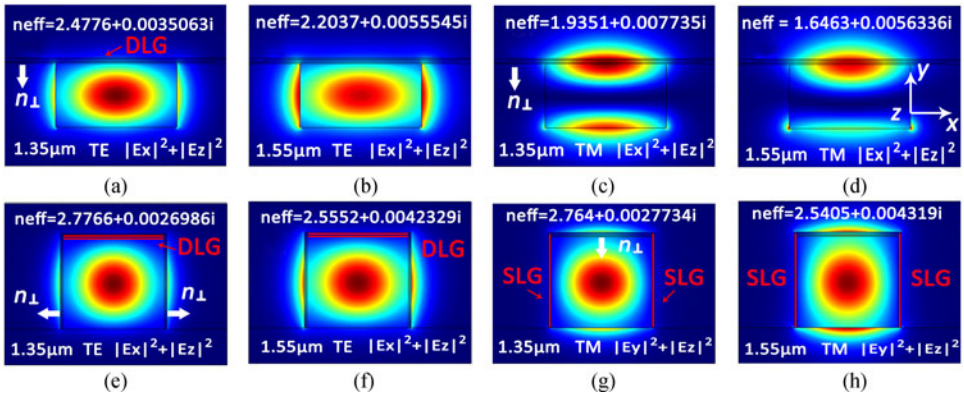

Fig. 11. (a)–(d) Distributions of tangential electric field intensity $|\boldsymbol{E}_{||}|^2$ in the buried waveguide structure with dual graphene layers [sketched as Fig. 3(c)]. The waveguide dimension is 400 nm $\times$ 225 nm at fixed $\mu = 0$ eV. (a) and (b) Distributions of $|\boldsymbol{E}_{||}|^2$ for the TE mode at 1.35 and 1.55 μm, respectively. (c) and (d) The same for the TM mode. (e)–(f) Distribution of $|\boldsymbol{E}_{||}|^2$ for the 400 nm $\times$ 380 nm convex strip waveguide structure [sketched as Fig. 3(a)] at $\mu = 0$ eV. DLG sandwiched by hBN spacer layers are paved on top of the waveguide. The side walls are coated by SLGs. For DLG $|\boldsymbol{E}_{||}|^2 = |\boldsymbol{E}_x|^2 + |\boldsymbol{E}_z|^2$, while for the two SLGs $|\boldsymbol{E}_{||}|^2 = |\boldsymbol{E}_y|^2 + |\boldsymbol{E}_z|^2$.

unfortunately exhibit distinctive dispersions in absorption, making this design no longer valid when incident wavelengths are aloof from 1550 nm. Fig. 10(b) and (c) illustrate the deviations in Im(n_{eff}) and optical loss for the 400 nm $\times$ 225 nm cross-sectioned design. Consequently, the buried waveguide structure actually cannot realize polarization-independent modulators, as present wavelength division multiplexing (WDM) systems require versatile optical modulations for multiple wavelengths. Particular designs may achieve equivalent absorption rate at a given wavelength but expired for other wavelengths at low chemical potential.

The reason of the divergences lies in that the distribution of in-plan electric field $|\boldsymbol{E}_{||}|$ exhibits different variation trends between TE and TM mode. Fig. 11(a)–(d) compare the distributions of $|\boldsymbol{E}_{||}|$ at $\lambda = 1350$ nm and 1550 nm for the two fundamental modes of $\mu = 0$ eV. Under the coordinates illustrated in Fig. 11(d), the in-plane electric field intensity can be formulated as $|\boldsymbol{E}_{||}|^2 = |\boldsymbol{E}_x|^2 + |\boldsymbol{E}_z|^2$. For TE mode, the x component of the electric field $\boldsymbol{E}_x$ is dominating. A longer optical wavelength λ leads to a weaker mode confinement and increased intensity of $|\boldsymbol{E}_{||}|^2$ in graphene, leaving a longer evanescent tail outside the side walls of the buried waveguide. Hence, the modulator exhibits stronger amplitude attenuation for TE mode at longer wavelengths, as shown in Fig. 10(c). However, the preferable component $\boldsymbol{E}_y$ of TM mode does not induce absorptions in graphene [19], [43], [44]. Thus the z component $\boldsymbol{E}_z$ mainly contributes to $|\boldsymbol{E}_{||}|$. By comparing Fig. 11(c) and (d), it can be noticed that the intensity of $|\boldsymbol{E}_z|^2$ at the top interface between the waveguide and graphene layers decreases at longer wavelengths. Therefore, the absorption of TM mode declines with the increment of signal wavelength around 1550 nm.

Consequently, despite that the buried waveguide configurations can marry the aforementioned advantages, it cannot well realize amplitude modulators that are not sensitive to polarization states. To realize broadband polarization-independent modulators for future on-chip interconnects, the distribution of $|\boldsymbol{E}_{||}|$ for TE mode must vary at same pace with TM mode across a certain band of wavelengths. Hence, the convex strip waveguide structure, sketched in Fig. 3(a), may have the potential. By properly designing the waveguide dimension (see Section 3 of the Supplementary Material), polarization-independent optical absorption can be achieved. As is shown in Fig. 11(e) and (f), in a 400 nm $\times$ 380 nm waveguide, the dominating electric filed component $\boldsymbol{E}_x$ of TE mode can effectively interact with the double layer graphene (DLG) on top of the convex strip waveguide but makes no contributions to the single-layered graphene (SLG) flakes coated on side walls. By contrast, the main component $\boldsymbol{E}_y$ for TM mode will no longer remain futile but induce absorptions

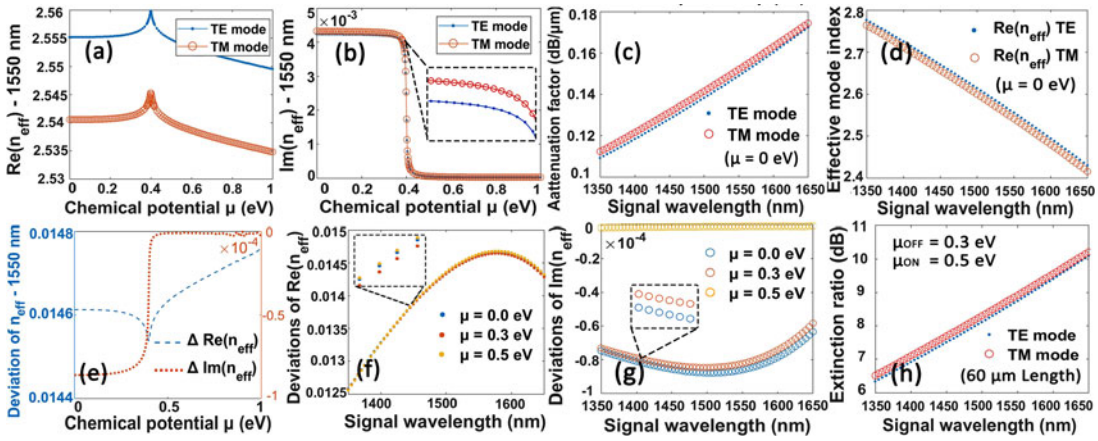

Fig. 12. Polarization-independent modulators for 400 nm × 380 nm convex strip waveguide [structure sketched as Fig. 3(a)]. (a) and (b) Re(n_{eff}) and Im(n_{eff}) as a function of μ for fundamental TE and TM modes. (c) and (d) Attenuation factor and Re(n_{eff}) versus λ for TE and TM modes at $\mu = 0$ eV. (e) The discrepancies of Re(n_{eff}) and Im(n_{eff}) between TE and TM modes. (f) and (g) Deviations between the two fundamental modes for Re(n_{eff}) and Im(n_{eff}), respectively. (h) Extinction ratio as a function of λ between the operation points. The "ON" state is assigned as $\mu_{\text{ON}} = 0.5$ eV and "OFF" state as $\mu_{\text{OFF}} = 0.3$ eV.

in both of the SLGs (instead of DLG). The z component $\boldsymbol{E}_z$ still exerts influence on both SLGs and DLG. Therefore, equivalent mode overlaps and optical absorptions can be attained for convex strip waveguide structure.

Fig. 12(a) and (b) illustrate the variations of the real and imaginary parts of n_{eff} for fundamental TE and TM mode at $\mu = 0$ eV, where very approaching values of Im(n_{eff}) is observed between the two orthogonal polarization states. Moreover, the modulation discrepancies are kept at low value across a broad wavelength range from 1.35 to 1.65 μm, as shown in Fig. 12(c) and (d). The corresponding divergences in n_{eff} as a function of chemical potential μ are calculated in Fig. 12(e) and (f), where the ΔIm(n_{eff}) is kept at the order of 10^{-5}. Moreover, if we set $\mu_{\text{OFF}} = 0.3$ eV as an operation point to achieve '0' signal and $\mu_{\text{ON}} = 0.5$ eV as another to obtain the '1' signal, polarization-independent modulators can be achieved. Fig. 12(h) illustrates the variations of the extinction ratio (ER) for TE and TM mode in a 60 μm waveguide, and an ER of 9 dB is achieved at $\lambda = 1.55$ μm (ER is defined as the ratio of light intensity between the two operation points μ_{ON} and μ_{OFF}; see Section 3 in Supplementary Material). Although the ER decreases at shorter wavelengths (originating from elevated mode confinements), the divergence is still kept close between the two fundamental modes.

5. Device Performance

5.1 Power Consumption

Low power dissipation is of vital significance to chip-scale optical interconnects. Considering a random data sequence, where the '0' and '1' bits possess equal possibility of occurrence, the average power consumption per bit E_{bit} can be estimated [20] (see Section 4 of the Supplementary Material). Generally, a smaller area of the overlapped graphene flakes S, smaller isolation layer thickness d_{s1}, bigger spacer layer permittivity ε_r and Fermi velocity v_F will contribute to low energy consumption. Moreover, if the graphene samples are pre-doped to approach a desired original doping level μ_g, the E_{bit} may be further decreased.

Table 1 shows the calculated results of E_{bit} for the aforementioned devices, where the Fermi velocity v_F can be engineered by modifying the graphene-integrated environment [63], [64]. For the proposed phase modulators of TM mode, graphene films are artificially doped to shift μ_g to a

TABLE 1
Device Performance Estimations

Application examples	Active length L (μm)	μ_g (eV)	v_F [63], [64] (m/s)	U_0 (V)	U_1 (V)	E_{bit} (pJ/bit)	f_{3dB} (GHz)
Phase modulation (Same structure as Fig. 8)	87.8 (TE mode)	0.77	1.7×10^6	−3.0	3.0	0.528	106.4
			2.5×10^6	−1.4	1.4	0.115	
	98.5 (TM mode)	0.77	1.7×10^6	−3.0	3.0	0.737	84.6
			2.5×10^6	−1.4	1.4	0.161	
Amplitude modulation (Same structure as Fig. 12)	60.0	0.42	1.7×10^6	−0.61	0.52	0.012	106.4
			2.5×10^6	−0.30	0.25	0.003	

high value like 0.77 eV (though it is actually difficult to precisely control the value of μ_g) when the bias voltage is not applied. The operation points are set as $\mu_{2\pi} = 1.0$ eV and $\mu_0 = 0.42$ eV, which corresponds for a phase shift of -2π and 0 respectively. The energy consumptions are estimated as 0.115 and 0.161 pJ/bit for the TE and TM mode phase modulators respectively.

Meanwhile, for the polarization-independent amplitude modulator of Fig. 12, the power consumption can be as low as 3.1 fJ/bit, arising from the optimized μ_g, ameliorated v_F and operation points ($\mu_0' = 0.3$ eV and $\mu_1' = 0.5$ eV for the '0' and '1' signals respectively). One may consider if these estimations are rather optimistic which is deviated from manufacture reality. However, with properly designed operation points and static calibration voltage, the power dissipation can still be kept at low level for the proposed polarization-independent amplitude modulator. Further discussions are made in Supplementary Material.

5.2 Operation Speed

Thanks to the ultrahigh carrier mobility of graphene, the electrical bandwidth is mainly limited by the parasitic response of the device [18], [19]. The 3 dB bandwidth of graphene-based waveguide modulators can be formulated as $f_{3dB} = 1/(2\pi RC)$ [9], where R is the device resistance and C stands for the total capacitance that is estimated via C_g. In the design and fabrication process, the resistance of graphene-metal contact deserves attention [67]. Meanwhile, the electrodes are supposed to be positioned at a distance from the waveguide (depending on the length of evanescent tail, typically 500–600 nm for 1550 nm wavelength) to prevent additional absorption, leaving the optical mode undisturbed. The device resistance is mainly comprised of the contact resistance R_c and sheet resistance of graphene R_s [12], [54],

$$R = 2R_s \times \frac{w_g}{L} + \frac{2R_c}{L} \tag{6}$$

where w_g is the effective width of graphene; L is the active length. $R_s = 200\ \Omega/\square$ [68], $R_c = 100\ \Omega\cdot\mu$m [61] are adopted. Calculation details are elaborated in Supplementary Material. The estimated 3 dB electrical bandwidths for the exemplary proposals are listed as Table 1 as well, where approximate

100 GHz modulation bandwidth can be expected and can be further ameliorated by modifying graphene's electrical contacts [69]. Besides, the operation speed and power consumption tend to counteract each other, and are both sensitive to the spacer layer thickness. The f_{3dB} can also be improved by introducing a thicker isolation layer between dual graphene flakes at a cost of increased power consumption.

6. Conclusion

By solely tailoring the dimensions of graphene-laminated photonic waveguides, the phase, amplitude and polarization of the fundamental propagating modes can be manipulated with flexibilities at different applied voltages. Here, a comprehensive analysis upon graphene-integrated Si waveguides is presented. We ascribe different device functionalities, including phase/amplitude modulators and polarizers, into the design and optimization of graphene-coupled waveguide dimensions. Considering actual fabrication feasibility and complexity, buried waveguides with graphene-on-graphene capacitor configuration is the promising and cost-effective choice. By maximizing $\Delta\mathrm{Re}(n_{\mathrm{eff}})$, compact phase modulators can be achieved, where a 2π phase shift is achieved in an active length of 87.8 μm for fundamental TE mode and 98.5 μm for TM mode with dual graphene layers. The optimal waveguide dimensions of our proposal are 400 nm $\times$ 180 nm and 500 nm $\times$ 260 nm for TE and TM mode respectively. The corresponding power consumptions are 115 fJ/bit (TE) and 161 fJ/bit (TM); the 3 dB electrical bandwidth are 106 GHz and 85 GHz accordingly.

At the absence of electrodes, broadband TE- or TM-pass polarizers are available, by tailoring waveguide dimensions to maximize the divergence: $\mathrm{Im}(n_{\mathrm{eff}})_{\mathrm{TE}} - \mathrm{Im}(n_{\mathrm{eff}})_{\mathrm{TM}}$. The extinction ratios are 18.0 dB and 18.6 dB for TE- and TM-pass polarizers respectively. With metalized electrical contacts, polarization switches can also be attained, where the applied voltages are utilized to control the attenuation or not for a specific polarization state. Moreover, the strong polarization-dependent optical absorption can also be exploited to realize amplitude modulators. We verified that polarization-independent optical modulators cannot be virtually realized in the proposed buried waveguide architecture, but possible for the convex strip waveguide structures. Under a waveguide dimension of 400 nm $\times$ 380 nm, the discrepancy of $\mathrm{Im}(n_{\mathrm{eff}})$ between the two fundamental modes are kept at an order of 10^{-5} over a broad wavelength band from 1.35 to 1.65 μm. An ER of 9 dB is achieved in an active length of 60 μm at $\lambda = 1.55$ μm.

Furthermore, the proposal can be switched between phase modulation ($|\mu|$ is tuned to block interband transitions) and amplitude modulation (μ is tuned around $\hbar\omega/2$) at different bias voltages. Design trade-offs are discussed. Power consumption and electrical bandwidth are evaluated as well, paving the way for the future applications of graphene-assisted photonic waveguide devices for optoelectronic integrations.

References

[1] Q. L. Bao and K. P. Loh, "Graphene photonics, plasmonics, and broadband optoelectronic devices," *ACS Nano*, vol. 6, pp. 3677–3694, 2012.
[2] G. T. Reed, G. Mashanovich, F. Y. Gardes, and D. J. Thomson, "Silicon optical modulators," *Nature Photon.*, vol. 4, pp. 518–526, 2010.
[3] Y. C. Shen *et al.*, "Deep learning with coherent nanophotonic circuits," *Nature Photon.*, vol. 11, pp. 441–446, 2017.
[4] A. S. Liu *et al.*, "A high-speed silicon optical modulator based on a metal-oxide-semiconductor capacitor," *Nature*, vol. 427, pp. 615–618, 2004.
[5] Q. F. Xu, B. Schmidt, S. Pradhan, and M. Lipson, "Micrometre-scale silicon electro-optic modulator," *Nature*, vol. 435, pp. 325–327, 2005.
[6] M. R. Watts, J. Sun, C. D. Rose, D. C. Trotter, R. W. Young, and G. N. Nielson, "Adiabatic thermo-optic Mach–Zehnder switch," *Opt. Lett.*, vol. 38, pp. 733–735, 2013.
[7] W. C. Chiu, C. C. Chang, J. M. Wu, M. Lee, and J. M. Shieh, "Optical phase modulators using deformable waveguides actuated by micro-electro-mechanical systems," *Opt. Lett.*, vol. 36, pp. 1089–1091, 2011.
[8] J. F. Liu *et al.*, "Waveguide-integrated, ultralow-energy GeSi electro-absorption modulators," *Nature Photon.*, vol. 2, pp. 433–437, 2008.
[9] K. Kim, J. Y. Choi, T. Kim, S. H. Cho, and H. J. Chung, "A role for graphene in silicon-based semiconductor devices," *Nature*, vol. 479, pp. 338–344, 2011.

[10] D. A. B. Miller, "Optical interconnects to silicon," *IEEE J. Sel. Topics Quantum Electron.*, vol. 6, no. 6, pp. 1312–1317, Nov./Dec. 2000.
[11] A. K. Geim and I. V. Grigorieva, "Van der Waals heterostructures," *Nature*, vol. 499, pp. 419–425, 2013.
[12] F. Bonaccorso, Z. Sun, T. Hasan, and A. C. Ferrari, "Graphene photonics and optoelectronics," *Nature Photon.*, vol. 4, pp. 611–622, 2010.
[13] K. S. Novoselov *et al.*, "Two-dimensional gas of massless Dirac fermions in graphene," *Nature*, vol. 438, pp. 197–200, 2005.
[14] L. Britnell *et al.*, "Strong light-matter interactions in heterostructures of atomically thin films," *Science*, vol. 340, pp. 1311–1314, 2013.
[15] S. Q. Yan *et al.*, "Slow-light-enhanced energy efficiency for graphene microheaters on silicon photonic crystal waveguides," *Nature Commun.*, vol. 8, 2017, Art. no. 14411.
[16] E. Hendry, P. J. Hale, J. Moger, and A. K. Savchenko, "Coherent nonlinear optical response of graphene," *Phys. Rev. Lett.*, vol. 105, 2010, Art. no. 097401.
[17] A. H. Castro Neto, F. Guinea, N. M. R. Peres, K. S. Novoselov, and A. K. Geim, "The electronic properties of graphene," *Rev. Modern Phys.*, vol. 81, pp. 109–162, 2009.
[18] J. Yan, Y. B. Zhang, P. Kim, and A. Pinczuk, "Electric field effect tuning of electron-phonon coupling in graphene," *Phys. Rev. Lett.*, vol. 98, 2007, Art. no. 166802.
[19] M. Liu *et al.*, "A graphene-based broadband optical modulator," *Nature*, vol. 474, pp. 64–67, 2011.
[20] M. Liu, X. B. Yin, and X. Zhang, "Double-layer graphene optical modulator," *Nano Lett.*, vol. 12, pp. 1482–1485, 2012.
[21] M. Midrio *et al.*, "Graphene-assisted critically-coupled optical ring modulator," *Opt. Exp.*, vol. 20, pp. 23144–23155, 2012.
[22] Y. Meng, R. G. Lu, Y. Shen, Y. Liu, and M. Gong, "Ultracompact graphene-assisted ring resonator optical router," *Opt. Commun.*, vol. 405, pp. 73–79, 2017.
[23] Q. L. Bao *et al.*, "Broadband graphene polarizer," *Nature Photon.*, vol. 5, pp. 411–415, 2011.
[24] X. Yin, T. Zhang, L. Chen, and X. Li, "Ultra-compact TE-pass polarizer with graphene multilayer embedded in a silicon slot waveguide," *Opt. Lett.*, vol. 40, pp. 1733–1736, 2015.
[25] R. E. P. Oliveira and C. J. S. Matos, "Graphene based waveguide polarizers: in-depth physical analysis and relevant parameters," *Sci. Rep.*, vol. 5, 2015, Art. no. 16949.
[26] T. Mueller, F. Xia, and P. Avouris, "Graphene photodetectors for high-speed optical communications," *Nature Photon.*, vol. 4, pp. 297–301, 2010.
[27] S. Goossens *et al.*, "Broadband image sensor array based on graphene–CMOS integration," *Nature Photon.*, vol. 11, pp. 366–371, 2017.
[28] F. Wang *et al.*, "Gate-variable optical transitions in graphene," *Science*, vol. 320, pp. 206–209, 2008.
[29] K. S. Novoselov *et al.*, "Electric field effect in atomically thin carbon films," *Science*, vol. 306, pp. 666–669, 2004.
[30] Z. Z. Ma, M. H. Tahersima, S. Khan, and V. J. Sorger, "Two-dimensional material-based mode confinement engineering in electro-optic modulators," *IEEE J. Sel. Topics Quantum Electron.*, vol. 23, no. 1, Jan./Feb. 2017, Art. no. 3400208.
[31] L. Ren *et al.*, "Terahertz and infrared spectroscopy of gated large-area graphene," *Nano Lett.*, vol. 12, pp. 3711–3715, 2012.
[32] G. W. Hanson, "Dyadic Green's functions and guided surface waves for a surface conductivity model of graphene," *J. Appl. Phys.*, vol. 103, 2008, Art. no. 064302.
[33] T. Stauber, N. M. R. Peres, and A. K. Geim, "Optical conductivity of graphene in the visible region of the spectrum," *Phys. Rev. B*, vol. 78, 2008, Art. no. 085432.
[34] Z. L. Lu and W. S. Zhao, "Nanoscale electro-optic modulators based on graphene-slot waveguides," *J. Opt. Soc. Amer. B*, vol. 29, pp. 1490–1496, 2012.
[35] J. Gosciniak and D. T. H. Tan, "Theoretical investigation of graphene-based photonic modulators," *Sci. Rep.*, vol. 3, 2013, Art. no. 01897.
[36] S. W. Ye, Z. S. Wang, L. F. Tang, Y. L. Zhang, R. G. Lu, and Y. Liu, "Electro-absorption optical modulator using dual-graphene-on-graphene configuration," *Opt. Exp.*, vol. 22, pp. 26173–26180, 2014.
[37] Y. T. Hu *et al.*, "Broadband 10 Gb/s operation of graphene electro-absorption modulator on silicon," *Laser Photon. Rev.*, vol. 10, pp. 307–316, 2016.
[38] S. J. Koester and M. Li, "Waveguide-coupled graphene optoelectronics," *IEEE J. Sel. Topics Quantum Electron.*, vol. 20, no. 1, Jan./Feb. 2014, Art. no. 6000211.
[39] A. B. Kuzmenko, E. van Heumen, F. Carbone, and D. van der Marel, "Universal optical conductance of graphite," *Phys. Rev. Lett.*, vol. 100, 2008, Art. no. 117401.
[40] A. Vakil and N. Engheta, "Transformation optics using graphene," *Science*, vol. 332, pp. 1291–1293, 2011.
[41] X. S. Li *et al.*, "Large-area synthesis of high-quality and uniform graphene films on copper foils," *Science*, vol. 324, pp. 1312–1314, 2009.
[42] K. S. Kim *et al.*, "Large-scale pattern growth of graphene films for stretchable transparent electrodes," *Nature*, vol. 457, pp. 706–710, 2009.
[43] M. S. Kwon, "Discussion of the epsilon-near-zero effect of graphene in a horizontal slot waveguide," *IEEE Photon. J.*, vol. 6, no. 3, Jun. 2014, Art. no. 6100309.
[44] W. L. Gao, J. Shu, C. Y. Qiu, and Q. F. Xu, "Excitation of plasmonic waves in graphene by guided-mode resonances," *ACS Nano*, vol. 6, pp. 7806–7813, 2012.
[45] R. Hao, W. Du, H. S. Chen, X. F. Jin, L. Z. Yang, and E. P. Li, "Ultra-compact optical modulator by graphene induced electro-refraction effect," *Appl. Phys. Lett.*, vol. 103, 2013, Art. no. 061116.
[46] C. H. Park, Y. Li, Y. W. Son, M. L. Cohen, and S. G. Louie, "Anisotropic behaviours of massless Dirac fermions in graphene under periodic potentials," *Nature Phys.*, vol. 4, pp. 213–217, 2008.
[47] C. T. Phare, Y. H. D. Lee, J. Cardenas, and M. Lipson, "Graphene electro-optic modulator with 30 GHz bandwidth," *Nature Photon.*, vol. 9, pp. 511–514, 2015.

[48] M. Asghari and A. V. Krishnamoorthy, "Silicon photonics energy-efficient communication," *Nature Photon.*, vol. 5, pp. 268–270, 2011.
[49] Y. Tan, R. Y. He, C. Cheng, D. Wang, Y. X. Chen, and F. Chen, "Polarization-dependent optical absorption of MoS2 for refractive index sensing," *Sci. Rep.*, vol. 4, 2014, Art. no. 7523.
[50] S. W. Ye *et al.*, "Polarization-independent modulator by partly tilted graphene-induced electro-absorption effect," *IEEE Photon. Technol. Lett.*, vol. 29, no. 1, pp. 23–26, Jan. 2017.
[51] R. Hao, W. Du, E. P. Li, and H. S. Chen, "Graphene assisted TE/TM-independent polarizer based on Mach–Zehnder interferometer," *IEEE Photon. Technol. Lett.*, vol. 27, no. 10, pp. 1112–1115, May 2015.
[52] L. Z. Yang *et al.*, "Low-chirp high-extinction-ratio modulator based on graphene–silicon waveguide," *Opt. Lett.*, vol. 38, pp. 2512–2515, 2013.
[53] M. Midrio, P. Galli, M. Romagnoli, L. C. Kimerling, and J. Michel, "Graphene-based optical phase modulation of waveguide transverse electric modes," *Photon. Res.*, vol. 2, pp. 34–39, 2014.
[54] S. W. Ye, F. Yuan, X. H. Zou, M. K. Shah, R. G. Lu, and Y. Liu, "High-speed optical phase modulator based on graphene-silicon waveguide," *IEEE J. Sel. Topics Quantum Electron.*, vol. 23, no. 1, Jan./Feb. 2017, Art. no. 3400105.
[55] G. Kovacevic and S. Yamashita, "Waveguide design parameters impact on absorption in graphene coated silicon photonic integrated circuits," *Opt. Exp.*, vol. 24, pp. 3584–3591, 2016.
[56] J. A. Dionne, K. Diest, L. A. Sweatlock, and H. A. Atwater, "PlasMOStor: A metal-oxide-Si field effect plasmonic modulator," *Nano Lett.*, vol. 9, pp. 897–902, 2009.
[57] Y. Lee *et al.*, "Wafer-scale synthesis and transfer of graphene films," *Nano Lett.*, vol. 10, pp. 490–493, 2010.
[58] J. W. Suk *et al.*, "Transfer of CVD-grown monolayer graphene onto arbitrary substrates," *ACS Nano*, vol. 5, pp. 6916–6924, 2011.
[59] M. Yankowitz *et al.*, "Emergence of superlattice Dirac points in graphene on hexagonal boron nitride," *Nature Phys.*, vol. 8, pp. 382–386, 2012.
[60] Y. D. Gao *et al.*, "High-speed electro-optic modulator integrated with graphene-boron nitride heterostructure and photonic crystal nanocavity," *Nano Lett.*, vol. 15, pp. 2001–2005, 2015.
[61] H. Zhong *et al.*, "Realization of low contact resistance close to theoretical limit in graphene transistors," *Nano Res.*, vol. 8, pp. 1669–1679, 2015.
[62] J. H. Wülbern *et al.*, "Electro-optic modulation in slotted resonant photonic crystal heterostructures," *Appl. Phys. Lett.*, vol. 94, 2009, Art. no. 241107.
[63] C. Hwang *et al.*, "Fermi velocity engineering in graphene by substrate modification," *Sci. Rep.*, vol. 2, 2012, Art. no. 590.
[64] C. H. Park, F. Giustino, C. D. Spataru, M. L. Cohen, and S. G. Louie, "Angle-resolved photoemission spectra of graphene from first-principles calculations," *Nano Lett.*, vol. 9, pp. 4234–4239, 2009.
[65] X. Hu and J. Wang, "Ultrabroadband compact graphene-silicon TM-pass polarizer," *IEEE Photon. J.*, vol. 9, no. 2, Apr. 2017, Art. no. 7101310.
[66] J. T. Kim and C. G Choi, "Graphene-based polymer waveguide polarizer," *Opt. Exp.*, vol. 20, pp. 3557–3562, 2012.
[67] F. Xia, V. Perebeinos, Y. M. Lin, Y. Wu, and P. Avouris, "The origins and limits of metal–graphene junction resistance," *Nature Nanotechnol.*, vol. 6, pp. 179–184, 2011.
[68] W. W. Cai, Y. W. Zhu, X. S. Li, R. D. Piner, and R. S. Ruoff, "Large area few-layer graphene/graphite films as transparent thin conducting electrodes," *Appl. Phys. Lett.*, vol. 95, 2009, Art. no. 123115.
[69] S. De and J. N. Coleman, "Are there fundamental limitations on the sheet resistance and transmittance of thin graphene films," *ACS Nano*, vol. 4, pp. 2713–2720, 2010.